JASA ARTICLE

Analysis of geometric defects in square locally resonant phononic crystals: A comparative study of modeling approaches[a)]

L. Katch,[1] M. Moghaddaszadeh,[2,b)] C. L. Willey,[3,c)] A. T. Juhl,[3] M. Nouh,[2,b)] and A. P. Argüelles[1,d)]
[1]*Department of Engineering Science and Mechanics, The Pennsylvania State University, University Park, Pennsylvania 16802, USA*
[2]*Department of Mechanical and Aerospace Engineering, University at Buffalo (State University New York), Buffalo, New York 14260, USA*
[3]*The Air Force Research Laboratory, Wright-Patterson Air Force Base, Dayton, Ohio 45433, USA*

ABSTRACT:
Phononic crystals can develop defects during manufacturing that alter the desired dynamic response and bandgap behavior. This frequency behavior change can enable successful defect inspection if the characteristic defect response is known. In this study, the behavior of a defective square unit cell comprising a freed and shortened leg is studied using a wave finite element method and an approximate continuous-lumped model to elucidate the defect induced qualitative dynamical features. These metrics are a computationally inexpensive alternative to modeling a defective unit cell within a large pristine array entirely in finite elements. The accuracy of these models is validated by comparing the result to a full finite element model. The impact of a shortened unit cell leg on the behaviors of an infinite array of defective cells and a finite array with a single defect are successfully predicted through dispersion curves and frequency response functions, respectively. These methods reveal defect-induced modes that split the local resonance bandgap of the pristine cell, as well as new anti-resonances resulting from the shortened leg. The study uses both approaches to evaluate the effect of defects in complex phononic crystal geometries and provides a comparative evaluation of the results of each model. © *2023 Acoustical Society of America.*
https://doi.org/10.1121/10.0022330
(Received 25 May 2023; revised 13 September 2023; accepted 18 October 2023; published online 14 November 2023)
[Editor: Vladislav Sergeevich Sorokin] Pages: 3052–3061

I. INTRODUCTION

Phononic crystals are structures formed by a tessellation of unit cells that inhibit or facilitate wave propagation (Brillouin, 1953; Kadic *et al.*, 2019; Phani *et al.*, 2006). The dispersive properties of a phononic crystal lattice are highly customizable through size, geometry, and material properties (Hussein *et al.*, 2014; Phani, 2017; Surjadi *et al.*, 2019). However, their sensitive frequency response implies that manufacturing defects have the potential to strongly influence their intended behavior (Rahman *et al.*, 2018). Defects can be purposefully placed to alter band gaps, often by resizing or removing portions of a unit cell (Bilal and Hussein, 2011; Colombi *et al.*, 2014; Oudich *et al.*, 2023; Sigalas, 1997), or induce bandgap resonances by truncating periodic lattices at select locations (Al Ba'ba'a *et al.*, 2017, Al Ba'ba'a *et al.*, 2023; Bastawrous and Hussein, 2022). Depending on geometric complexity, this defect analysis can be modeled simply as a connected-mass model or as intricately as a full finite element model with multiple degrees of freedom to design for desired band gaps (Bilal and Hussein, 2011; Diaz *et al.*, 2005; Oudich *et al.*, 2023). Alternatively, these techniques can be used to characterize changes in the desired pristine frequency behavior resulting from undesirable manufacturing defects, such as irregular unit cell geometries, missing or fractured components, non-uniform microstructures, and material distribution (Rahman *et al.*, 2018; Silva and Gibson, 1997). The rise in additive manufacturing enables the fabrication of increasingly complicated phononic crystals and furthers the need for defect characterization (Kennedy *et al.*, 2019; Lu *et al.*, 2022; Montgomery *et al.*, 2020). Selecting the appropriate level of complexity for modeling defective cells and understanding the trade-off in accuracy and computational costs will improve the efficiency of defect characterization. A comparative study between various methods with increasing complexity for defect characterization is performed herein.

For complicated phononic crystal structures, the wave finite element method (WFEM) is often used (Zhou *et al.*, 2015). This method involves modeling a unit cell within finite element software like COMSOL or ABAQUS to construct the transfer matrix, **T**, which relates applied loads and displacements from one location to another (Mace *et al.*, 2005). The eigenvalues of the transfer matrix provide the dispersion curves with real and imaginary wavenumbers, κ, across a range of frequencies (often known as the *driven* wave

[a)]This paper is part of a special issue on Wave Phenomena in Periodic, Near-periodic, and Locally Resonant Systems.
[b)]Also at: Department of Civil, Structural and Environmental Engineering, University at Buffalo (SUNY), Buffalo, NY 14260, USA.
[c)]Also at: UES, Inc., Dayton, OH 45432, USA.
[d)]Email: arguelles@psu.edu

https://doi.org/10.1121/10.0022330

approach), which is beneficial compared to a Floquet-Bloch theorem approach that is limited to producing dispersion curves with real κ (Junyi and Balint, 2015; Mead, 1996) (*free* wave approach). Constructing the complete dispersion curves using WFEM for pristine and defective unit cells can provide the overall effect of the defects on the band gaps (Kharrat *et al.*, 2014a,b). The transfer matrix, **T**, may also be used to predict responses of arrays combining a defective cell with a set of pristine cells through **T** multiplication (Nayfeh, 1991; Wang *et al.*, 2010). However, these techniques present numerical challenges for complex finite element models as they contain very large and very small values. As an alternative, the finite array can be modeled in a full finite element model (FEM). The distinction is made between WFEM, which uses a set of prescribed loading conditions and displacements on a single unit cell to construct a transfer matrix, and FEM, which uses an array of unit cells. For FEM, by modeling more degrees of freedom with finite elements, all modes, including torsional, can be studied with the penalty of additional computational expense.

Simplified and approximate models of reduced order can be desirable to retain the computational efficiency but provide necessary stability for application of the transfer matrix approach (Waki *et al.*, 2009). On the simplest level, phononic crystals can be modeled as a mass-spring network. Mass-spring lumped element modeling provides a simplified understanding of the underlying physics and dispersive behavior, both at the unit cell level as well as the vibrational modes of the finite realization, and has even been expanded to three-dimensional systems (Lucklum and Vellekoop, 2018). Conventional mass-spring modeling does not employ torsional springs; therefore, torsional modes are not defined through this technique. For improved descriptions of vibrations, a coupled mass-spring and continuum model can be used. Depending on the nature of the problem, the continuum portion can be described via closed-form or finite element formulations. For example, combined beam and mass-spring models have been used to interpret the dissipative mechanics of one-dimensional flexural metamaterials (Liu and Hussein, 2012; Yu *et al.*, 2006) and those with inertant networks (Aladwani *et al.*, 2022a). Similarly, combined plate and mass-spring models have been used to elucidate fluid-structural coupling in periodic structures adjacent to acoustic cavities (Aladwani *et al.*, 2019), and most recently to accelerate dispersion calculations for non-classically damped, two-dimensional phononic materials (Aladwani *et al.*, 2022b).

This work examines WFEM and approximate mass-spring modeling as computationally efficient alternatives to full FEM for defect characterization. The selected unit cell, an aluminum square unit cell comprised of four legs extending from a central point of connection, and defect, a shortened and freed leg, were inspired by the cross-shaped honeycomb of Phani *et al.* (2006). This unit cell and corresponding defect were selected because of their collective ability to be modeled using both approximate and WFEM approaches. Thus, this configuration is well-posed to serve as a model system for analyzing the advantages and limitations of the utilized methods, with the modeling approaches being generalizable to other unit cell and defect configurations. The trade-off between the modeling approaches for defect characterization is analyzed using dispersion curves and finite model outputs.

Within this paper, the setup is first described in Sec. II, followed by the framework for each modeling technique: WFEM in Sec. II A, FEM used for validation in Sec. II B, and the approximate mass-spring model in Sec. II C. With the modeling methods established, the results for defect characterization through WFEM generated dispersion curves are analyzed in Sec. III A. Next, using the approximate model, the finite array outputs are found by transfer matrices and explored in Sec. III B and pole-zero analysis is conducted for a five-cell array with a center pristine or defective unit cell. Last, the results are compared to a full FEM finite array with a defective unit cell used as the ground truth for the defective behavior in Sec. III C.

II. MODEL PARAMETERS AND SETUP

The selected lattice has a square shape, which is commonly found in the literature (Chen *et al.*, 2017; Cheng *et al.*, 2020; Phani *et al.*, 2006; Trainiti *et al.*, 2016) and is modeled herein with unit cell length, $a = 0.5$ m, width of 0.05 m, and thickness of 0.01 m using aluminum (Young's modulus $E = 70$ GPa, Poisson's ratio $\nu = 0.33$, and density $\rho = 2700\,\mathrm{kg/m^3}$), shown in Fig. 1(A). The surfaces of the unit cell legs not connected along the axis of wave propagation, x, are fixed. As stated before, this unit cell configuration was selected to demonstrate a geometry feasible for both full FEM and the approximate beam-spring-mass model to emphasize the compatibility of each method. Defects for the unit cell included a freed leg at a 10% and 20% shortened length. In the following, the finite element and approximate models used for analysis are described in detail.

A. Wave finite element model

The unit cell was modeled using the finite element method in COMSOL 6.0. The model used a hexagonal element size of 0.005 m, so each leg was 100 elements long and the thickness included two elements. Using frequency domain analysis, the unit cell was loaded with unit magnitude forces and moments to create a transfer matrix that could subsequently be used for dispersion analysis. Four individual loading conditions: two shear loads, $V_{L,R}$, and two bending moments, $M_{L,R}$, where the subscripts L and R denote the left and right ends, respectively, were employed. This combination of loads enabled the out-of-plane displacements to be well captured, as illustrated in Fig. 1(A). Defects were modeled by freeing the top leg of the unit cell and shortening it by 10% and 20%, as shown in Fig. 1(C). By running a frequency sweep from 100 to 2000 Hz, the resulting out-of-plane displacements, v, and angle, $\theta = dv/dx$, were found on either end of the unit cell for the pristine and defective cases.

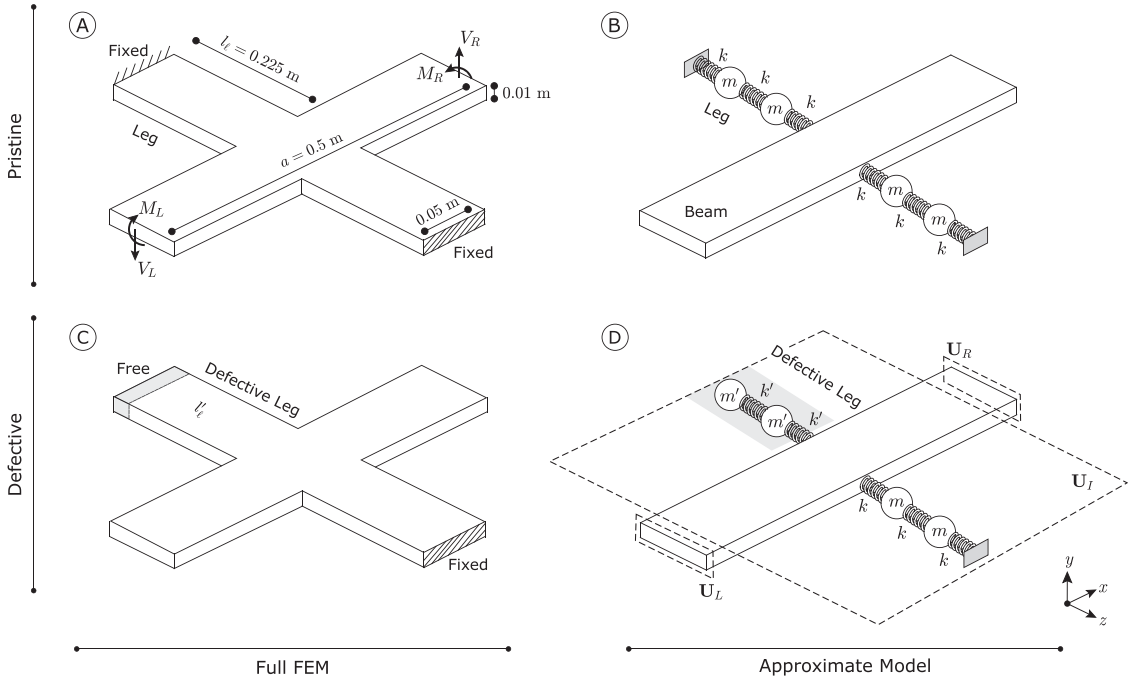

FIG. 1. Details of the unit cell: (A) The unit cell is a square lattice with two fixed legs. For WFEM, four individual loading conditions on the square unit cell are simulated. (B) The approximate model uses a series of lumped masses and springs for the vertical bars (legs) of the unit cell and a beam model for the horizontal bar of the unit cell. (C) For WFEM, the defect is a shortened and freed leg. (D) For the approximate model, the leg defect is modeled by adjusting the mass-spring parameters as well as the boundary condition of the shortened leg.

By defining a unit cell displacement vector $\mathbf{u}_u = [v_L, \theta_L, v_R, \theta_R]^T$ and a forcing vector $\mathbf{F}_u = [V_L, M_L, V_R, M_R]^T$, the combinations of four loading scenarios and four displacements result in a 4×4 matrix of inputs and outputs defined as the receptance matrix, $\mathbf{H}$,

$$\mathbf{u}_u = \mathbf{H}\mathbf{F}_u. \tag{1}$$

The receptance matrix can be broken into its square block submatrices,

$$\mathbf{H} = \begin{bmatrix} \mathbf{H}_{LL} & \mathbf{H}_{LR} \\ \mathbf{H}_{RL} & \mathbf{H}_{RR} \end{bmatrix}, \tag{2}$$

and reconfigured into the transfer matrix, $\mathbf{T}$, given by

$$\mathbf{T} = \begin{bmatrix} \mathbf{H}_{RR}\mathbf{H}_{LR}^{-1} & \mathbf{H}_{RL} - \mathbf{H}_{RR}\mathbf{H}_{LR}^{-1}\mathbf{H}_{LL} \\ \mathbf{H}_{LR}^{-1} & -\mathbf{H}_{LR}^{-1}\mathbf{H}_{LL} \end{bmatrix}. \tag{3}$$

The transfer matrix relates the left and right sides of the unit cell using the displacements and forces,

$$\mathbf{Y}_R = \mathbf{T}\mathbf{Y}_L, \tag{4}$$

where $\mathbf{Y}_{L,R} = [V_{L,R}, M_{L,R}, v_{L,R}, \theta_{L,R}]^T$. Solving the eigenvalue problem of the transfer matrix enables calculations of dispersion,

$$[\mathbf{T} - \lambda\mathbf{I}]\phi = \mathbf{0}, \tag{5}$$

where $\lambda = e^{-i\kappa a}$ is the phase associated with propagation of the Bloch wave and $\phi = \mathbf{Y}_L$. The eigenvalues, λ, of the transfer matrix from Eq. (5) can be used to construct the dispersion curves by solving for $\lambda = e^{-i\kappa a}$, where a is the length of the waveguide's unit cell. A real-valued frequency is used as an input to solve for the corresponding complex-valued Bloch wavenumber, κ. Section III A presents the dispersion curves for the pristine and defective cases obtained from the WFEM method.

B. Finite element model: Finite array calculations

The displacements calculated from the mass-spring model enable visualization of finite arrays with a small computational load; nevertheless, the model contains simplified displacements. Therefore, it can be advantageous to construct the full, higher fidelity model in COMSOL, despite the large computational load. The finite array of $n = 5$ unit cells, assuming ideal connections between unit cells, is modeled in COMSOL 6.0. The center unit cell is replaced with the 10% shorter or 20% shorter unit cells to understand the effect of the defect on the finite array. The input leg is excited using a unit magnitude shear force and the output displacement, v, from the opposite leg is extracted directly from COMSOL.

C. Approximate model

To develop a simplified model of the square unit cell shown in Fig. 1(A), which captures the structure's fundamental dynamics efficiently, a horizontal beam is modeled using 30 one-dimensional, 2-node Euler-Bernoulli beam elements, each containing 4 degrees of freedom. The perpendicular legs are approximated using a series of identical

https://doi.org/10.1121/10.0022330

lumped masses m connected via identical springs of stiffness k, as shown in Fig. 1(B). In the pristine case, the legs are modeled using 2 masses and 3 springs on each side of the horizontal beam and are fixed on both ends. The values of m and k are extracted from the leg's geometry and material properties, such that $m = \rho A l_\ell/2$ and $k = 12EI/(l_\ell/3)^3$, where $l_\ell = 0.225$ m is the leg's length for the pristine case. The mass and stiffness components of the upper and lower legs are coupled with the corresponding beam elements at the junction where the legs meet the base structure at the mid-span of the unit cell. The unit cell mass and stiffness matrices, $\mathbf{K}_u$ and $\mathbf{M}_u$, respectively, are then assembled from the combination of the beam and the approximated mass-spring legs. Fixed boundary conditions are applied to the top and bottom degrees of freedom of the upper and lower legs to mimic the square lattice in Fig. 1(A).

To capture the effect of the defect, the pristine model transitions to the defective one by setting the upper leg free and updating the values of m and k to m' and k' to account for leg shortening, as illustrated in Fig. 1(D). For example, for a defective unit cell with a 10% shorter leg, the values $l'_\ell = 0.9 l_\ell = 0.203$ m and $m' = \rho A l'_\ell/2$ can be calculated accordingly. We note that the combination of m' and k' is unique for a given defect geometry; e.g., we are not able to find a scenario in which a narrower defective leg results in the same combination of m' and k' corresponds to a shorter defective leg.

1. Dispersion calculations

The periodic boundary conditions and dispersion analysis are based on the formulation developed in the literature (Aladwani and Nouh, 2020; Phani *et al.*, 2006), summarized here. We consider a Bloch-wave solution of the form

$$\mathbf{u}_u(x,t) = \tilde{\mathbf{u}}_u(x) e^{i(\omega t + \kappa x)}, \tag{6}$$

where $\mathbf{u}_u(x,t)$ is the unit cell displacement vector as a function of location and time, ω is the angular frequency, κ is the wavenumber, and $\tilde{\mathbf{u}}_u(x)$ is a periodic amplitude. Two discretized displacement vectors are then introduced as follows:

$$\mathbf{U}^T = \begin{bmatrix} \mathbf{U}_L^T & \mathbf{U}_I^T & \mathbf{U}_R^T \end{bmatrix}, \tag{7a}$$

$$\tilde{\mathbf{U}}^T = \begin{bmatrix} \mathbf{U}_L^T & \mathbf{U}_I^T \end{bmatrix}, \tag{7b}$$

where $\mathbf{U}_L$, $\mathbf{U}_I$, and $\mathbf{U}_R$ denote the displacements of left, internal, and right degrees of freedom, respectively, as indicated in Fig. 1(D). While $\mathbf{U}$ contains the nodal displacements of all degrees of freedom in the unit cell discretization, $\tilde{\mathbf{U}}$ only contains the displacements of the minimal set of degrees of freedom sufficient for Bloch boundary conditions. We can then relate these two using the Bloch periodicity matrix $\mathbf{P}(\kappa)$ such that $\mathbf{U} = \mathbf{P}(\kappa)\tilde{\mathbf{U}}$, where

$$\mathbf{P}(\kappa) = \begin{bmatrix} \mathbf{I} & \mathbf{0} \\ \mathbf{0} & \mathbf{I} \\ \mathbf{I}e^{i\kappa a} & \mathbf{0} \end{bmatrix}. \tag{8}$$

Here, a is unit cell length, and $\mathbf{I}$ and $\mathbf{0}$ denote identity and zero matrices, respectively. The reduced mass $\tilde{\mathbf{M}}_u$ and stiffness $\tilde{\mathbf{K}}_u$ matrices are then

$$\tilde{\mathbf{M}}_u = \mathbf{P}'\mathbf{M}_u\mathbf{P}, \tag{9a}$$

$$\tilde{\mathbf{K}}_u = \mathbf{P}'\mathbf{K}_u\mathbf{P}, \tag{9b}$$

where $\mathbf{P}'$ is the complex conjugate transpose of $\mathbf{P}$. Consequently, the equations of motion can be cast in the form of an eigenvalue problem as follows:

$$[\tilde{\mathbf{K}}_u(\kappa) - \omega^2\tilde{\mathbf{M}}_u(\kappa)]\tilde{\mathbf{U}} = \mathbf{0}. \tag{10}$$

The unit cell dispersion curves can be computed by solving this eigenvalue problem for a range of κ values spanning the irreducible Brillouin zone.

2. Finite array calculations

To perform frequency response analysis of a finite array comprised of a one-dimensional series of the approximate beam-spring-mass cells, global mass and stiffness matrices are obtained by assembling $\mathbf{M}_u$ and $\mathbf{K}_u$ for $n = 5$ unit cells. Following this, a transfer function relating the out-of-plane displacement of the right end of the array to its counterpart on the left is computed over the frequency range of interest.

III. RESULTS

Using the WFEM model, the dispersion curves are evaluated for the defective cases. Next, the approximate model is used to construct the output for a finite array containing defective and pristine cells. This approach is also used to conduct pole-zero analysis and parametrically vary the shortened leg length. Last, these results are compared to the FEM model of the finite array. Consistency is established between the methods, WFEM, FEM, and approximate model in the Appendix.

A. Defect evaluation via dispersion curves

The dispersion curves are created using WFEM, which includes more degrees of freedom than the approximate mass-spring model as detailed in the Appendix, and will, therefore, better capture defective behavior. The simple matrix operation of finding the dispersion curves by taking the eigensolutions of the transfer matrix using Eq. (3) lends itself to handling the numerical complexity of the WFEM output.

Dispersion curves were first constructed for the pristine unit cell and are illustrated in Fig. 2(A). Several band gaps are present ranging from 131–171 Hz, 346–413 Hz, 693–868 Hz, 984–1130, and 1464–1492 Hz. The imaginary wavenumber component displayed on the left side of Fig. 2(A) shows four of the aforementioned five band gaps to be of the Bragg type, as famously characterized by an attenuation constant of finite attenuation and a parabolic profile (Al Ba'ba'a *et al.*, 2023). However, the bandgap spanning the 984–1130 Hz range is revealed to be a local resonance bandgap as confirmed by (1) the 0 to π wavenumber shift in the bounding

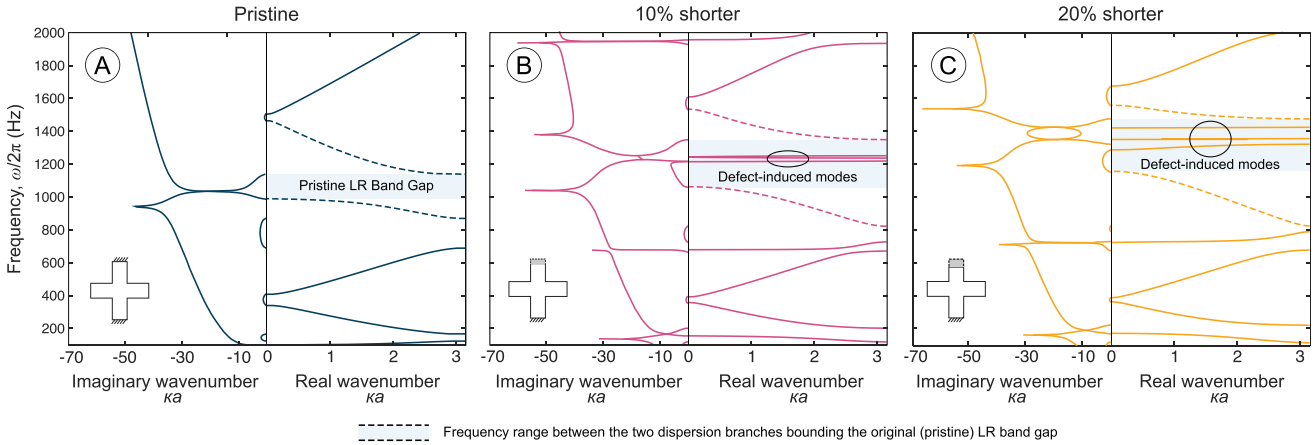

FIG. 2. (Color online) Dispersion curves with the primary bandgap of interest shaded for (A) a pristine aluminum square unit cell, (B) defective unit cell with a 10% shorter top leg, and (C) defective unit cell with a 20% shorter top leg.

dispersion branches on the real wavenumber side and (2) the sharp attenuation peaks sandwiched between the evanescent branches on the imaginary wavenumber side, consistent with previous literature on flexural locally resonant beams (Liu and Hussein, 2012; Yu *et al.*, 2006).

Band gaps have been shown to change in the presence of defects (Colombi *et al.*, 2014). This result can prove advantageous if purposefully placing defects for applications like energy harvesting; however, manufacturing defects are unlikely to occur exactly in each repeated unit cell; therefore, dispersion curve analysis is limited for applications with combinations of different unit cells. Figures 2(B) and 2(C) examine the dispersion diagrams of the two defective unit cells, a 10% and a 20% shorter, freed top leg, as shown in the schematic inset in each diagram. Several changes are brought about due to leg shortening, some of which may be used as indicative measures of the defect type and extent (i.e., shortening percentage). For example, an additional dispersion branch can be seen above the third dispersion branch in both cases. Other changes include the onset of a zero-frequency bandgap reminiscent of phononic crystals with elastic foundations (Al Ba'ba'a *et al.*, 2017) and the transition of one of the low-frequency Bragg band gaps to a resonant one. In the presence of complexities such as mixed-type band gaps, which show concurrent Bragg and resonance imaginary branches, it becomes challenging to pinpoint one bandgap and track its corresponding counterpart in the defective case. Instead, consider the range of frequencies covered by the two dispersion branches that bound the local resonance in the pristine unit cell in Fig. 2(A). These two branches are plotted via dashed lines for easy tracking and appear to maintain their shape throughout all three cases. Both Figs. 2(B) and 2(C) show the emergence of three narrow pass bands within this frequency range, which effectively breakup the original local resonance bandgap to a few smaller ones. This is intuitive since the unit cell's side branch legs play the resonators' role and are responsible for forming the clean local resonance bandgap in the pristine case. As such, it stands to reason that altering one of the two legs (in this case, freeing and shortening it) would instigate some new propagating modes, ones that likely correspond to resonant frequencies of the shortened legs which are close but move further apart as the defect increases, as shown by the increasing distance between these pass bands in the 20% case [Fig. 2(C)].

While these features are of interest since they provide a first impression of the effect of the defect on the underlying unit cell dispersion behavior, it should be emphasized that this dispersion diagram assumes an infinitely long array in which the same defect exists in each and every unit cell (i.e., a fully propagating defect). However, in practical applications, the defect is typically limited to a single unit cell within an otherwise non-defective array. The following sections illustrate how these defect-induced modes manifest themselves in the behavior of a finite array with a single defect through transfer function analysis.

B. Defect evaluation via transfer function of finite array

While numerical instabilities can inhibit transfer matrix modeling of finite arrays through WFEM, the approximate model provides the stability required to predict the displacements from finite arrays. Figure 3 summarizes the finite response for the defective case in which the middle upper leg is shortened by 10%, as obtained by the approximate model, detailed in Sec. II C. As can be seen in Fig. 3(A) the bandgap becomes narrower compared to the pristine case (which is highlighted in blue for comparison). More interestingly, an additional collocated resonance and anti-resonance pair emerges at 186 Hz, and another emerges at 1263 Hz, at the locations marked "1" and "2," respectively, in Fig. 3(A).

To confirm and track the emerging changes around and beyond the bandgap region of the defective system, a pole-zero map is constructed from the input-output transfer function of the underlying linear dynamical system and is shown in Fig. 3(B). The locations of poles (gray crosses) and zeros (red circles) in the vicinity of the bandgap region, displayed in Fig. 3(A), are mapped back to the frequency response curve and shown in the background using dashed gray and

https://doi.org/10.1121/10.0022330

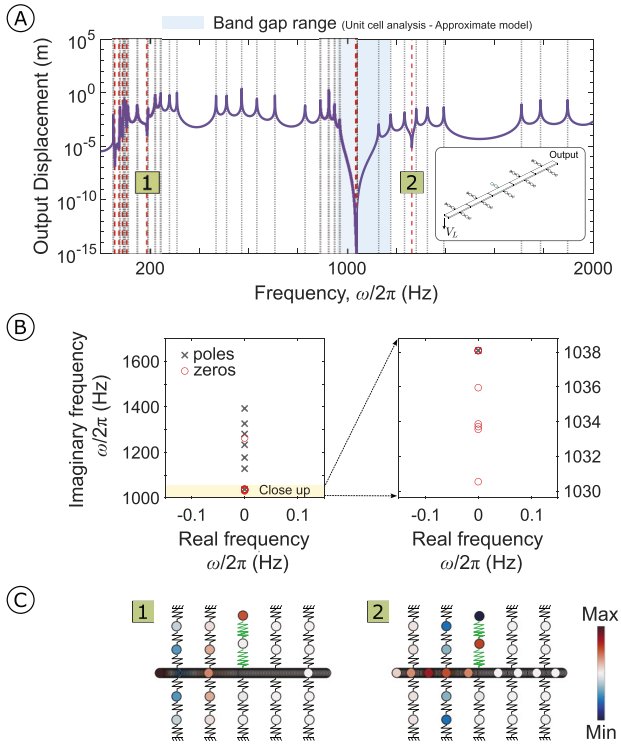

FIG. 3. (Color online) Evaluation of defect using finite array transfer function. (A) Transfer function for the defective case with five cells in which the middle upper leg is shortened by 10%. Poles and zeros are depicted with dashed gray and red lines. Band gap for the pristine case is shown with blue on the background. Additional pairs of resonance and anti-resonances are labeled with "1" and "2." (B) Poles and zeros in the vicinity of bandgap. (C) Out of plane displacement field for the array corresponding to frequencies associated with labels "1" and "2" in (A).

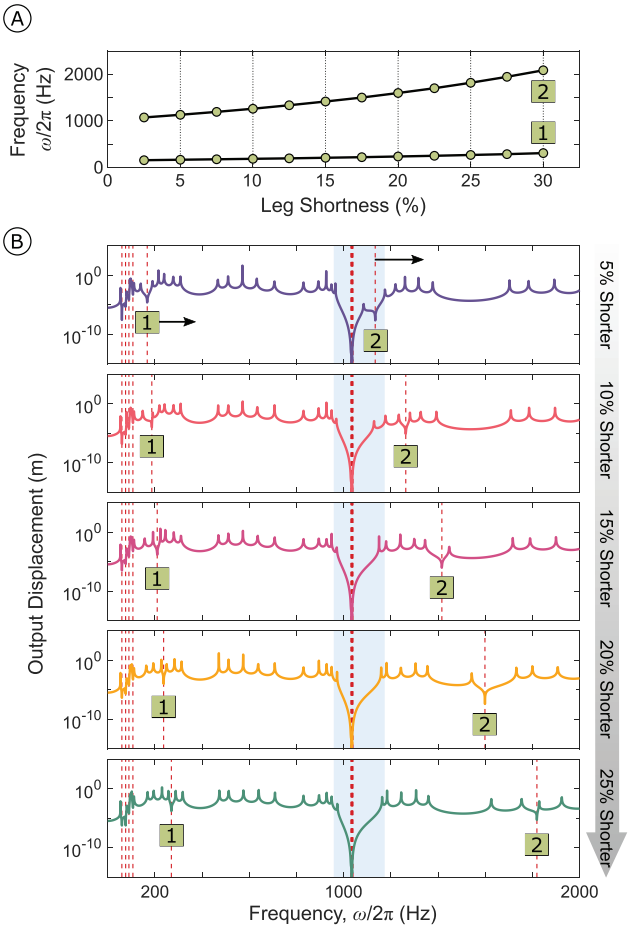

FIG. 4. (Color online) Parametric study by approximate model on the effect of gradually decreasing the shortened leg size in defective cases. (A) Comparison between the frequency of first (labeled with 1) and second (labeled with 2) resonance and anti-resonance pairs. (B) Frequency response of the cases highlighted with dashed line in (A).

red lines for poles and zeros, respectively. The frequency response and pole-zero maps shown in Figs. 3(A) and 3(B) provide two key observations about the influence of the shortened leg on the state of the system: the first is the spilling of two resonances inside the pristine bandgap range as evident by the two poles captured at approximately 1038 and 1130 Hz. Since a pole-zero cancellation takes place at 1038 Hz, as depicted in Fig. 3(B), only one of these two resonances appears as a distinct peak in the frequency response of Fig. 3(A) at 1130 Hz inside the shaded range. The second observation pertains to the multiplicity of zeros around the major bandgap anti-resonance as captured by the multiple red circles which appear at very closely spaced frequencies in the close-up subplot of Fig. 3(B), and culminate in the heavily attenuated output displacement inside the bandgap. This is a hallmark feature of resonance-based band gaps, as previously demonstrated in the literature (Al Ba'ba'a *et al.*, 2017). These zeros perfectly coincide in pure lumped parameter systems for which closed-form expressions for transfer function zeros can be obtained (Stein *et al.*, 2022), but are expected to show negligibly small deviations in any approximate numerical modeling approach, such as that used here.

The associated mode shapes are shown in Fig. 3(C) to further study these additional resonances and anti-resonances. Looking closely at the displacement pattern of the short defective leg (middle upper leg), it can be seen that the additional resonance and anti-resonance pairs are associated with the first [Fig 3(C), left] and second [Fig 3(C), right] mode shapes of the cantilever leg at 186 and 1263 Hz, respectively.

This method can be utilized to conduct a parametric study on leg length, as shown in Fig. 4. The decreasing size of the defective leg increases the frequency of its resonances, as seen in Fig. 4(A). Further, the frequency of the second defective resonance and anti-resonance pair (labeled with 2) increases faster than that of the first one (labeled with 1) as the leg length decreases. From a defect sizing perspective, this result means that higher mode shapes are more sensitive to defect size, acknowledging that experimental damping may cause slight attenuation of the resonant and anti-resonant peaks. In other words, these higher modes have larger jumps in frequency for a 5% increment change compared to the lower frequency anti-resonance. Figure 4(B) depicts the frequency response for leg shortness values highlighted with dashed lines in Fig. 4(A). It can be seen that the first resonance and anti-resonance pair of interest shifts to 167, 186, 210, 237, and 269 Hz for the leg lengths

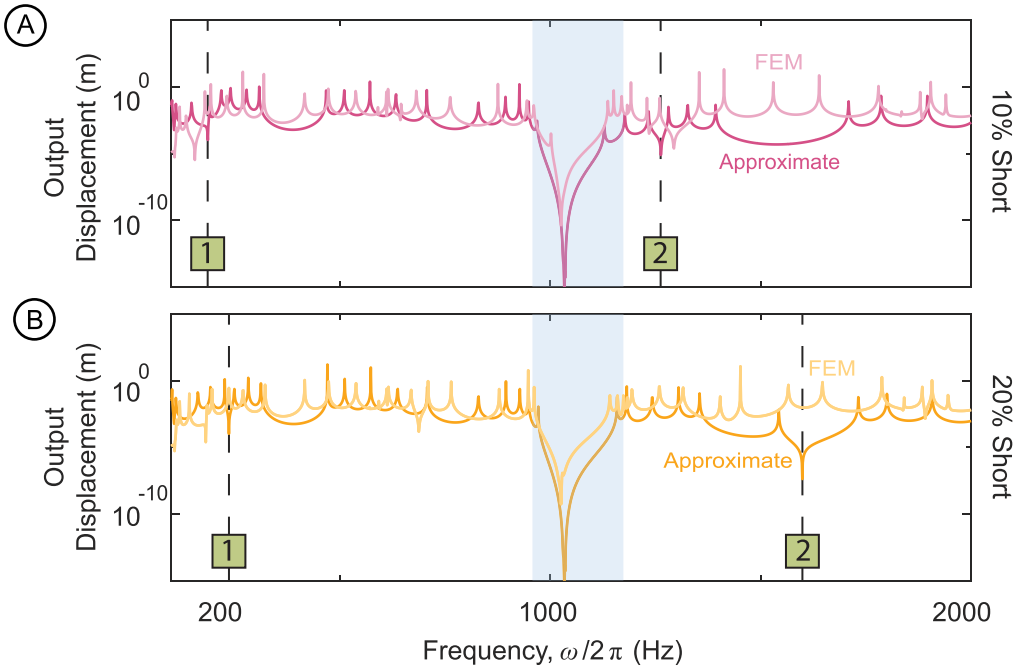

FIG. 5. (Color online) The out-of-plane displacements for a finite unit array with (A) 4 pristine unit cells and a 10% shorter leg center cell and (B) 4 pristine unit cells and a 20% shorter leg center cell. The anti-resonances corresponding to the approximate model are marked.

corresponding to a shortening of 5%, 10%, 15%, 20%, and 25%, respectively. Similarly, the second defective resonance and anti-resonance pair shifts to 1134, 1263, 1416, 1599, and 1819 Hz, respectively.

C. Defect evaluation via FEM finite array

The output displacements from the finite arrays of 5 unit cells with a varying center cell are shown in Fig. 5. As a whole, the approximate model captures the finite behavior well and predicts the resulting anti-resonances 1 and 2 for the 10% short case within 30 Hz and anti-resonance 1 for the 20% short case within 50 Hz. For the defective finite array case, the higher frequency COMSOL anti-resonance is affected by torsional modes, so it is slightly higher in frequency. This torsional behavior becomes increasingly significant as the leg decreases in size, causing greater discrepancies for the 20% shorter defective case, where the anti-resonance, labeled 2, around 1600 Hz moves outside of the 2000 Hz range plotted herein. Thus, for the currently freed shortened leg, the torsional behavior becomes a dominant component of the defective mode shapes and causes higher frequency discrepancies in the anti-resonances.

The predictive nature of the dispersion curves can be compared to the finite array. To start, the primary Bragg bandgap centered around 1000 Hz, was shown to shift higher in frequency for the defective cases. This behavior was representative of the finite structure having the bandgap widen for the defective cases. Additionally, the two key anti-resonances within the finite structure, labeled 1 and 2, can be mapped back to the differing pristine and defect imaginary dispersion curves. These anti-resonances are located at points where the mixed-mode crossing imaginary dispersion curves combine with the Bragg curves, resulting in a strong anti-resonant behavior. Again, anti-resonance 2 of the 20% short case is also not well defined by the dispersion curves, as they were also constructed without torsional behavior. Therefore, significant torsional behavior is outside the scope of the WFEM model generated dispersion curves.

The significant effect of torsional behavior within larger defect sizes is an important consideration for other configurations; i.e., if the effect of the defect on mode shape stays within the displacements well defined by the approximate model, then the approximate model serves as a strong alternative. If the defect drives mode shapes not included within the approximate model, then the estimated response is limited in accuracy. This diverging anti-resonance behavior between the FEM and approximate may not be as strong for other defects that maintain out-of-plane displacement mode shapes. These defective mode shapes and the degree of torsional or axial behavior will inform the differences between the two models when applied to cases outside those explored herein.

IV. CONCLUSIONS

Within the presented work, the effect of a shortened and freed leg on square unit cell behavior was examined through WFEM and approximate modeling approaches and compared to an FEM result. Through dispersion curve analysis using the WFEM model, the bandgap behavior was shown to change due to the decreasing leg size. The band gaps shift in frequency and are split by additional branches that arise and present regions of combined anti-resonant behavior. This analysis provided frequency ranges of interest but solely described the infinite behavior of a single unit cell type. Next, the resulting displacement from a finite

https://doi.org/10.1121/10.0022330

array was predicted using the approximate beam-mass-spring model. The low computational expense enabled a parametric study on defective leg length that showed anti-resonances shifting higher in frequency with decreasing leg size. The higher frequency anti-resonance shifted more as defect size changed, indicating that higher frequency inspection could prove useful in defect sizing. Last, this displacement result was compared to the computationally expensive COMSOL finite array model, which revealed some additional defective behavior as a result of torsional displacements that were only supported by the higher fidelity FEM model. The torsional displacements became increasingly significant as the defective leg decreased in size, causing discrepancies from the approximate model.

ACKNOWLEDGMENTS

This work is supported by the Air Force Office of Scientific Research under Grant No. 20RXCOR058, the National Science Foundation under Award No. 1847254, and through the Summer Faculty Fellowship Program (SFFP). Distribution Statement A: Approved for Public Release; Distribution is Unlimited. PA# AFRL-2023-2315.

APPENDIX: MODEL VALIDATION VIA ANALYSIS OF PRISTINE UNIT CELLS

In order to establish a comparison baseline between the WFEM and the approximate beam-mass-spring model, the dispersion curves are created using both approaches, as shown

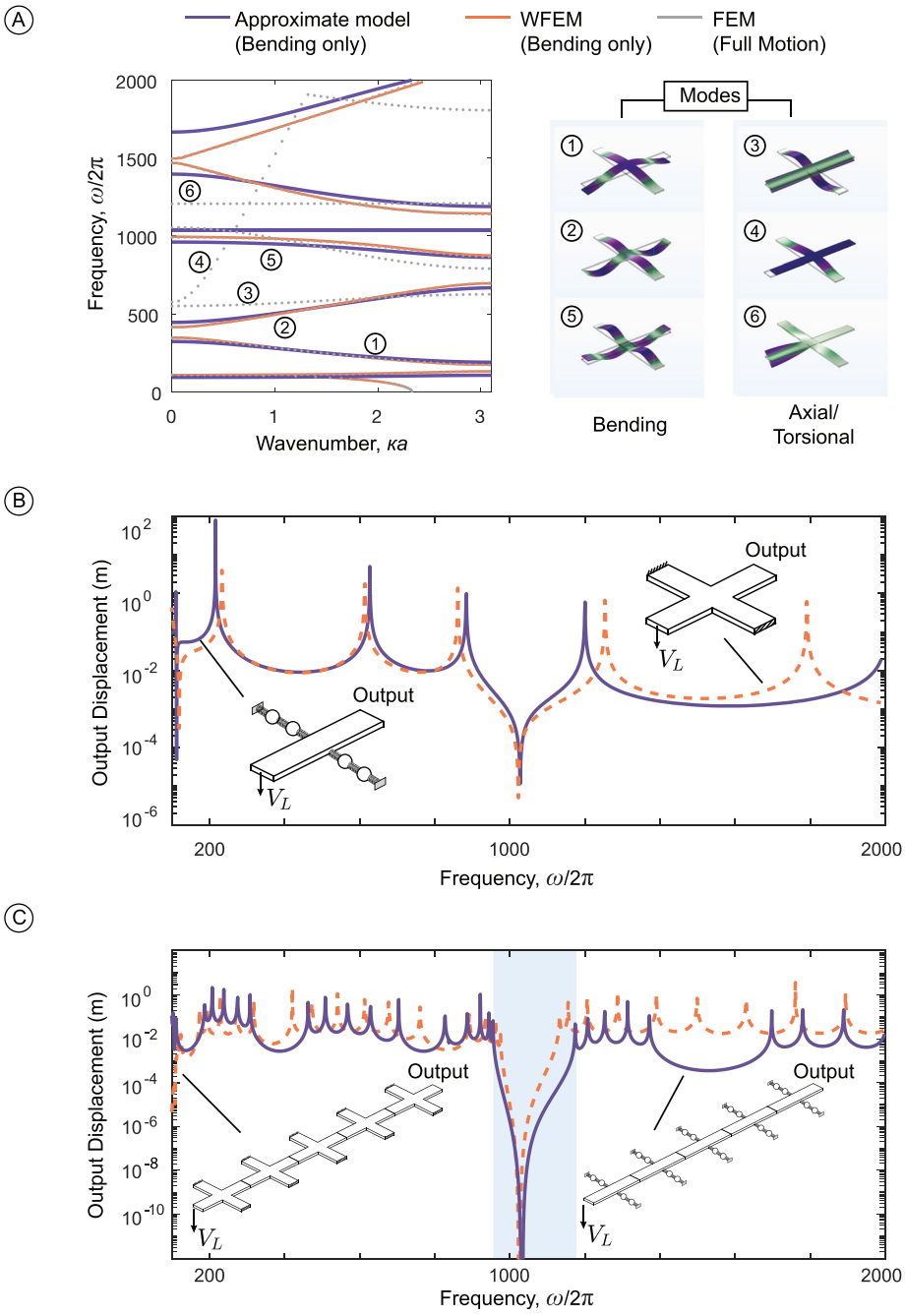

FIG. 6. (A) (Color online) The dispersion curves calculated for the pristine square unit cell shown in Fig. 1(A) using the FEM (Floquet-Bloch) method (gray), the WFEM eigenvalues method (red), and the approximate model shown in Fig. 1(B) (blue). The eigenmodes for branches 1–6 are shown on the right. The out-of-plane displacement amplitude caused by a shear loading on (B) a pristine square unit cell and (C) a finite array of 5 pristine square unit cells calculated using the direct FEM output and approximate modeling approaches.

in the left panel of Fig. 6(A). These dispersion curves are compared against a FEM Floquet-Bloch method. The approximate and WFEM models exclusively lend themselves to model bending modes, which represents a large portion of the dispersive behavior, while the Floquet-Bloch method shows modes of all motions. Both WFEM and approximate models capture the bending modes well when compared against the FEM Floquet-Bloch model. Nevertheless, the bottom-most band in the WFEM curves is not present within the other plots; a result of this method using a real-valued frequency as the input to solve for complex-valued wavenumber, which produces dispersion curves with κ values including imaginary components, indicative of decaying or evanescent waves. Some slight shifts within the band gaps of the WFEM and approximate curves are also present, as the WFEM model has more degrees of freedom (i.e., greater fidelity) than the latter, which closely captures bending modes (dispersion curves 1, 2, and 5) while not accounting for torsional (dispersion curves 3 and 6), axial (dispersion curve 4), and torsional coupled modes as shown in the right panel of Fig. 6(A).

Next, Fig. 6(B) shows the output displacement from an applied unit magnitude shear load for the FEM and approximate cases. The displacements provided by each method result in reasonably close relative displacement plots. At around 1800 Hz, an additional resonance arises from a torsional mode within the fixed leg, which is not represented in the beam-mass-spring model.

Last, Fig. 6(C) shows the output displacement for the FEM and approximate model of a finite one-dimensional pristine array made up of five cells connected in series in response to an input shear load V_L applied at the opposite end. While the two sets of curves generally agree, especially in terms of the major bandgap location and shared resonances, the FEM frequency response contains more resonant peaks, as one might expect, due to the ability of this model to capture more finite vibrational modes given the presence of additional degrees of freedom. It is worth noting that the shaded region in the figure represents the resonant bandgap range of the pristine structure as predicted by the unit cell dispersion analysis of the approximate model.

Aladwani, A., Almandeel, A., and Nouh, M. (**2019**). "Fluid-structural coupling in metamaterial plates for vibration and noise mitigation in acoustic cavities," Int. J. Mech. Sci. **152**, 151–166.

Aladwani, A., Mohammed, A., and Nouh, M. (**2022a**). "Tunable dissipation in elastic metamaterials via methodic reconfiguration of inertant mechanical networks," Meccanica **57**(6), 1337–1352.

Aladwani, A., and Nouh, M. (**2020**). "Mechanics of metadamping in flexural dissipative metamaterials: Analysis and design in frequency and time domains," Int. J. Mech. Sci. **173**, 105459.

Aladwani, A., Nouh, M., and Hussein, M. I. (**2022b**). "State-space bloch mode synthesis for fast band-structure calculations of non-classically damped phononic materials," Comput. Methods Appl. Mech. Eng. **396**, 115018.

Al Ba'ba'a, H., Nouh, M., and Singh, T. (**2017**). "Pole distribution in finite phononic crystals: Understanding Bragg-effects through closed-form system dynamics," J. Acoust. Soc. Am. **142**(3), 1399–1412.

Al Ba'ba'a, H. B., Willey, C. L., Chen, V. W., Juhl, A. T., and Nouh, M. (**2023**). "Theory of truncation resonances in continuum rod-based phononic crystals with generally asymmetric unit cells," Adv. Theory Simul. **6**(2), 2200700.

Bastawrous, M. V., and Hussein, M. I. (**2022**). "Closed-form existence conditions for bandgap resonances in a finite periodic chain under general boundary conditions," J. Acoust. Soc. Am. **151**(1), 286–298.

Bilal, O. R., and Hussein, M. I. (**2011**). "Ultrawide phononic band gap for combined in-plane and out-of-plane waves," Phys. Rev. E **84**(6), 065701.

Brillouin, L. (**1953**). *Wave Propagation in Periodic Structures: Electric Filters and Crystal Lattices* (Dover, Mineola, NY), Vol. 2.

Chen, Y., Li, T., Scarpa, F., and Wang, L. (**2017**). "Lattice metamaterials with mechanically tunable Poisson's ratio for vibration control," Phys. Rev. Appl. **7**(2), 024012.

Cheng, Q., Guo, H., Yuan, T., Sun, P., Guo, F., and Wang, Y. (**2020**). "Topological design of square lattice structure for broad and multiple band gaps in low-frequency range," Extreme Mech. Lett. **35**, 100632.

Colombi, A., Roux, P., and Rupin, M. (**2014**). "Sub-wavelength energy trapping of elastic waves in a metamaterial," J. Acoust. Soc. Am. **136**(2), EL192–EL198.

Diaz, A., Haddow, A., and Ma, L. (**2005**). "Design of band-gap grid structures," Struct. Multidisc. Optim. **29**, 418–431.

Hussein, M. I., Leamy, M. J., and Ruzzene, M. (**2014**). "Dynamics of phononic materials and structures: Historical origins, recent progress, and future outlook," Appl. Mech. Rev. **66**(4), 040802.

Junyi, L., and Balint, D. (**2015**). "An inverse method to determine the dispersion curves of periodic structures based on wave superposition," J. Sound Vib. **350**, 41–72.

Kadic, M., Milton, G. W., van Hecke, M., and Wegener, M. (**2019**). "3D metamaterials," Nat. Rev. Phys. **1**(3), 198–210.

Kennedy, J., Flanagan, L., Dowling, L., Bennett, G., Rice, H., and Trimble, D. (**2019**). "The influence of additive manufacturing processes on the performance of a periodic acoustic metamaterial," Int. J. Polym. Sci. **2019**, 7029143.

Kharrat, M., Ichchou, M., Bareille, O., and Zhou, W. (**2014a**). "Pipeline inspection using a torsional guided-waves inspection system. Part 1: Defect identification," Int. J. Appl. Mech. **06**(04), 1450034.

Kharrat, M., Ichchou, M., Bareille, O., and Zhou, W. (**2014b**). "Pipeline inspection using a torsional guided-waves inspection system. Part 2: Defect sizing by the wave finite element method," Int. J. Appl. Mech. **06**(04), 1450035.

Liu, L., and Hussein, M. I. (**2012**). "Wave motion in periodic flexural beams and characterization of the transition between Bragg scattering and local resonance," J. Appl. Mech. **79**, 011003.

Lu, C., Hsieh, M., Huang, Z., Zhang, C., Lin, Y., Shen, Q., Chen, F., and Zhang, L. (**2022**). "Architectural design and additive manufacturing of mechanical metamaterials: A review," Engineering. **17**, 44–63.

Lucklum, F., and Vellekoop, M. J. (**2018**). "Bandgap engineering of three-dimensional phononic crystals in a simple cubic lattice," Appl. Phys. Lett. **113**(20), 201902.

Mace, B. R., Duhamel, D., Brennan, M. J., and Hinke, L. (**2005**). "Finite element prediction of wave motion in structural waveguides," J. Acoust. Soc. Am. **117**(5), 2835–2843.

Mead, D. (**1996**). "Wave propagation in continuous periodic structures: Research contributions from southampton, 1964–1995," J. Sound Vib. **190**(3), 495–524.

Montgomery, S. M., Kuang, X., Armstrong, C. D., and Qi, H. J. (**2020**). "Recent advances in additive manufacturing of active mechanical metamaterials," Curr. Opin. Solid State Mater. Sci. **24**(5), 100869.

Nayfeh, A. H. (**1991**). "The general problem of elastic wave propagation in multilayered anisotropic media," J. Acoust. Soc. Am. **89**(4), 1521–1531.

Oudich, M., Gerard, N. J., Deng, Y., and Jing, Y. (**2023**). "Tailoring structure-borne sound through bandgap engineering in phononic crystals and metamaterials: A comprehensive review," Adv. Funct. Mater. **33**(2), 2206309.

Phani, A. S. (**2017**). *Elastodynamics of Lattice Materials* (Wiley, New York), Chap. 3, pp. 53–92.

Phani, A. S., Woodhouse, J., and Fleck, N. (**2006**). "Wave propagation in two-dimensional periodic lattices," J. Acoust. Soc. Am. **119**(4), 1995–2005.

Rahman, K. M., Hu, Z., and Letcher, T. (**2018**). "In-plane stiffness of additively manufactured hierarchical honeycomb metamaterials with defects," J. Manuf. Sci. Eng. **140**(1), 011007.

Sigalas, M. (**1997**). "Elastic wave band gaps and defect states in two-dimensional composites," J. Acoust. Soc. Am. **101**(3), 1256–1261.

Silva, M. J., and Gibson, L. J. (**1997**). "The effects of non-periodic microstructure and defects on the compressive strength of two-dimensional cellular solids," Int. J. Mech. Sci. **39**(5), 549–563.

Stein, A., Nouh, M., and Singh, T. (**2022**). "Widening, transition and coalescence of local resonance band gaps in multi-resonator acoustic metamaterials: From unit cells to finite chains," J. Sound Vib. **523**, 116716.

Surjadi, J. U., Gao, L., Du, H., Li, X., Xiong, X., Fang, N. X., and Lu, Y. (**2019**). "Mechanical metamaterials and their engineering applications," Adv. Eng. Mater. **21**(3), 1800864.

Trainiti, G., Rimoli, J. J., and Ruzzene, M. (**2016**). "Wave propagation in undulated structural lattices," Int. J. Solids Struct. **97-98**, 431–444.

Waki, Y., Mace, B., and Brennan, M. (**2009**). "Numerical issues concerning the wave and finite element method for free and forced vibrations of waveguides," J. Sound Vib. **327**(1-2), 92–108.

Wang, Y.-Z., Li, F.-M., Kishimoto, K., Wang, Y.-S., and Huang, W.-H. (**2010**). "Wave localization in randomly disordered layered three-component phononic crystals with thermal effects," Arch. Appl. Mech. **80**(6), 629–640.

Yu, D., Liu, Y., Wang, G., Zhao, H., and Qiu, J. (**2006**). "Flexural vibration band gaps in Timoshenko beams with locally resonant structures," J. Appl. Phys. **100**(12), 124901.

Zhou, C., Lainé, J., Ichchou, M., and Zine, A. (**2015**). "Wave finite element method based on reduced model for one-dimensional periodic structures," Int. J. Appl. Mech. **07**(02), 1550018.